Scientific Research Publishing

Journal of Geographic Information System, 2024, 16, 397-417
https://www.scirp.org/journal/jgis
ISSN Online: 2151-1969
ISSN Print: 2151-1950

Modelling and Mapping Likely Soil Rutting Occurrences across Forested Areas

Daniel Snow, Elizabeth White, Nana Agyei O. Afriyie, Paul A. Arp

Faculty of Forestry and Environmental Management, University of New Brunswick, Fredericton, New Brunswick, Canada
Email: arp1@unb.ca

How to cite this paper: Snow, D., White, E., Afriyie, N.A.O. and Arp, P.A. (2024) Modelling and Mapping Likely Soil Rutting Occurrences across Forested Areas. *Journal of Geographic Information System*, **16**, 397-417.
https://doi.org/10.4236/jgis.2024.166023

Received: November 13, 2024
Accepted: December 20, 2024
Published: December 23, 2024

Abstract

This article addresses where ruts are likely to occur during in-field forest operations. This was done by inspecting high-resolution surface images across New Brunswick (NB) and elsewhere to mark where ruts have (1) and have not (0) occurred in harvested cutblocks. This marking revealed 1) where off-road operations were likely done on moist to wet and unfrozen soils; and 2) whether the ruts so incurred were water-logged at the time of imaging. Through geospatial processing of the NB-wide digital elevation model (DEM, available at 1 m resolution), the following attributes were added to each of the marked rut and no-rut locations: 1) the cartographic depth-to-water (DTW) as referenced to the nearest flow channels with >1 and >4 ha upslope flow accumulation areas (FA); 2) the topographic position index (TPI) in reference to the mean annulus elevation 50 m away from each DEM cell; 3) mean slope and curvatures within each cell-surrounding 10-m circle; 4) the terrain wetness index (TWI); 5) soil association type according to the NB forest soil map, adjusted for NB's most recent hydrographic network delineations for waterbodies and wetlands. Subjecting these data to logistic regression analysis revealed that image-located off-road rutting occurred at about 90% probability in water-accumulating zones where TPI is <0 m and DTW is <1 m. Using slope, curvature, TWI, and soil type as additional rut occurrence predictors did not affect this zonation significantly.

Keywords

Forest Operations, Off-Road, Satellite Imageries, Rut Locations, Point Shapefiles, Logistic Regression Analysis, Rut Occurrence Projections

1. Introduction

Soil rutting due to off-road forest harvest and post-harvest operations is a widespread problem [1]-[5]. Rutting would primarily occur when operating on wet

and non-frozen soil conditions, as these would exist temporarily to permanently on drainage-challenged soils, *i.e.*, in depressed areas, on flat to slightly sloping land, and adjacent to temporary to permanent stream channels, wetlands, water bodies, and shores [6]-[9]. In general, soils are limited in resisting soil compaction as soil moisture approaches the plastic limit and decreases further towards water saturation ([10]-[13]. Where rutting cannot be avoided, soil compaction and displacement:

- reduce soil and flow-channel stabilities and increase soil erosion along slopes [14]-[18];
- lower water infiltration and air exchange which reduces root development and expected crop yields [19];
- increase in-field operation costs by slowing operations due to recovering rut-stalled machines, adding to machine maintenance costs, and requiring rut repair.

Since off-road soil trafficability can now be related to per-tire machine loads, tire/track footprints, number of machine passes along the same track, and soil type [20]-[22], it is now possible to determine when and where machines likely induce soil rutting, and how deep these ruts will be. Specifically, this can be done through [6] [23]:

- Forest hydrology modelling using daily weather records to simulate soil moisture conditions as these vary year-round.
- Topographic terrain modelling to address ridge-to-valley variations in vegetation and soil type. This modelling involves using and evaluating the following DEM-generated data layers at 1 m resolution for 1) the Terrain Wetness Index (TWI [24] [25]); 2) the Topographic Position Index (TPI [26]), and 3) the cartographic Depth-To-Water Index (DTW [27]). The derivation of these indices has been facilitated through the increasing availability of LiDAR-derived digital elevation models (DEMs) at, e.g., 1 m resolution.

Briefly, TWI, which indexes the D8-derived upslope flow accumulation for each DEM cell [28] in relation to the slope of that cell, increases towards flat and low-lying areas with increasing upslope watershed areas. TPI relates the elevation of any cell within the DEM raster to the mean elevation of its surrounding annulus at a specified radius [29]. The resulting numbers are, respectively, positive, zero, or negative where the cells lie above, at, or below their mean annulus elevations. The cartographic depth-to-water index (DTW) is determined by assessing the minimum ("least-cost") rise of the land away from weather-dependent open-water areas including temporal to permanent flow channels for which DTW is set to 0. This being so, soils along permanent open waters are considered to be:

- very poorly drained when DTW < 10 cm,
- poorly drained when 10 ≤ DTW < 25 cm,
- imperfectly drained when 25 ≤ DTW < 50 cm,
- moderately well drained when 50 ≤ DTW < 100 cm,
- well drained when 1 ≤ DTW < 20 m, and
- excessively well drained when DTW ≥ 20 m.

This article reports on developing practical and easy-to-use techniques that led to 1) marking where off-road traffic rutting has (1) or has not (0) occurred within forested cutblocks, and 2) to use this information to project where else such rutting is likely to occur in wet and unfrozen soils. This was done in three stages involving three areas of interest (**Figure 1**) dealing with an initial methodology exploration (AOE). This was followed by checking (AOM) and verifying (AOV) the approach. The process of doing so was facilitated using:

- ArcMap and ArcGIS Pro mapping software availability.
- High-resolution surface images (Google Earth, ESRI, and GeoNB surface imageries), spanning the course of 14 years (*i.e.*, 2010-2024), as available.
- Province-wide forest soil association map (http://www.snb.ca/geonb1/e/dc/catalogue-E.asp); see also [30]).
- Province-wide shapefiles of provincial boundary, water bodies, and wetlands (http://www.snb.ca/geonb1/e/dc/catalogue-E.asp);
- Province-wide LiDAR-generated 1-m resolution digital elevation model (DEM) (http://www.snb.ca/geonb1/e/dc/catalogue-E.asp) to derive the surface rasters for depression fill (FI), slope (SL), upslope flow accumulation (FA), DTW along ephemeral and/or permanent flow channels associated with FA > 1 and >4 ha, respectively, TPI, and TWI.

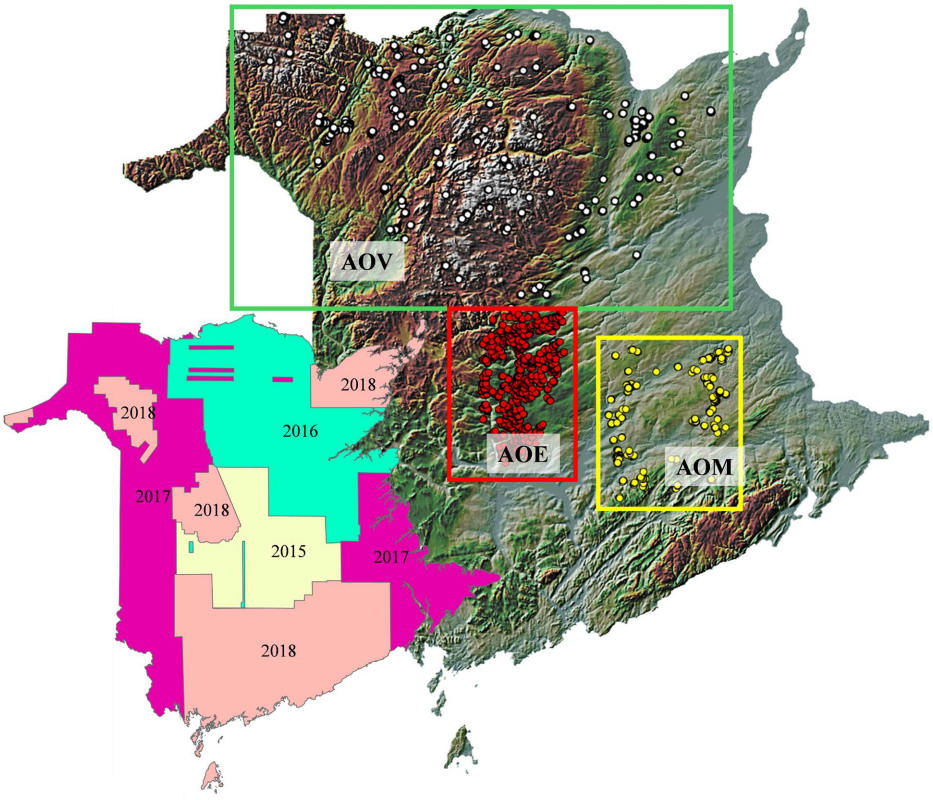

Figure 1. Overview of cutblock rut versus no-rut dot placements across three study areas in New Brunswick: AOE: exploration area (red); AOM: model-guided dot placements (yellow); AOV: model verification area (white); overlain on NB's hillshaded DEM at 1 m resolution. Also shown: extent of LiDAR DEM coverage by year.

The analytical processing involved logistically analyzing the binary rut and no-rut marks as the to-be-predicted variable, and the associated soil- and location-indexed Slope, Curvature, DTW, TPI, and TWI numbers as independent rut-predictor variables.

2. Methodology

2.1. Study Areas

The areas selected for image-based rut versus no-rut dot placements per cutblock are shown in Figure 1. Here, the AOE and AOV areas refer to image-recognized dot placements whereas the AOM area refers to model-adjusted dot placements. As is the case for most of New Brunswick, these areas are mostly covered by glacial deposits in the form of ablation and basal tills permeated by streams, wetlands, lakes, and floodplain sediments. The soils, as per the New Brunswick Forest Soil map, vary by 1) texture (from sandy to silty and clayey), 2) rooting depth (<15 to >100 cm), and organic matter and coarse fragment type and contents. The topography varies from flat to rolling and hummocky. Soil moisture conditions vary by slope position, season, weather, soil texture, organic matter content, and drainage. Annually, these areas receive about 1100 mm of precipitation. Mean daily temperatures range from −10˚C in January to 19˚C in July. Elevations across the areas vary from 0 - 820 m above sea level.

2.2. Rut versus No-Rut Dot Placements

Harvest blocks within each of the AOE, AOV, and AOM areas were used for rut versus no-rut marking using high-resolution GeoNB, ESRI, Bing, and 2000-2020 Historical Google Earth imageries. To maximize visual detection, only images with sharp post-harvest appearances were selected. The marking then focussed on dark and presumably water-filled rut lines along single-pass harvest trails, as visible at 1:500 to 1:2000 image resolution. The within-cutblock rut locations were marked as per Table 1, and this was done in conjunction with selecting and verifying an equal number of no-rut locations nearby (Figure 2). For this process, only cutblocks with sharp post-harvest rut appearances were selected, and locations with remaining ambiguity (e.g., tree shadows, dark slash piles) were discarded (Figure 3). Also discarded were ruts along multi-pass tracks, done to locate single-pass ruts where soils would be 1) least resistant to rut-induced soil compaction and soil displacement, and 2) appeared to be water-filled and therefore black at imaging time. Inspecting the same cutblock across successive Google Earth images revealed that rut presence faded and disappeared over time as ruts dried out and/or became overgrown.

Figure 4 affirms that off-road water-filled ruts were easily image-located shortly after harvesting but were not fully LiDAR-DEM resolved 3 years thereafter. In contrast, roads, trails, and multi-pass tracks would continue to be image- and DEM-traceable for longer periods of time. To further ensure rut and no-rut marking precision, each point was reinspected such that 1) rut locations were moved

to their nearest rut-patch centers, and 2) no-rut locations were moved at least 30 m away from these patches, as needed. Each rut and no-rut location was subsequently marked 1 and 0, respectively, and the associated x and y coordinates were point-shapefile registered. The number of rutting and non-rutting points per harvest block varied from 2 to 14, mostly depending on harvest block size and the number of isolated rut patches within. Altogether, doing so generated a total of 4800 post-harvest rut and no-rut locations across the AOE, AOV, and AOM study areas.

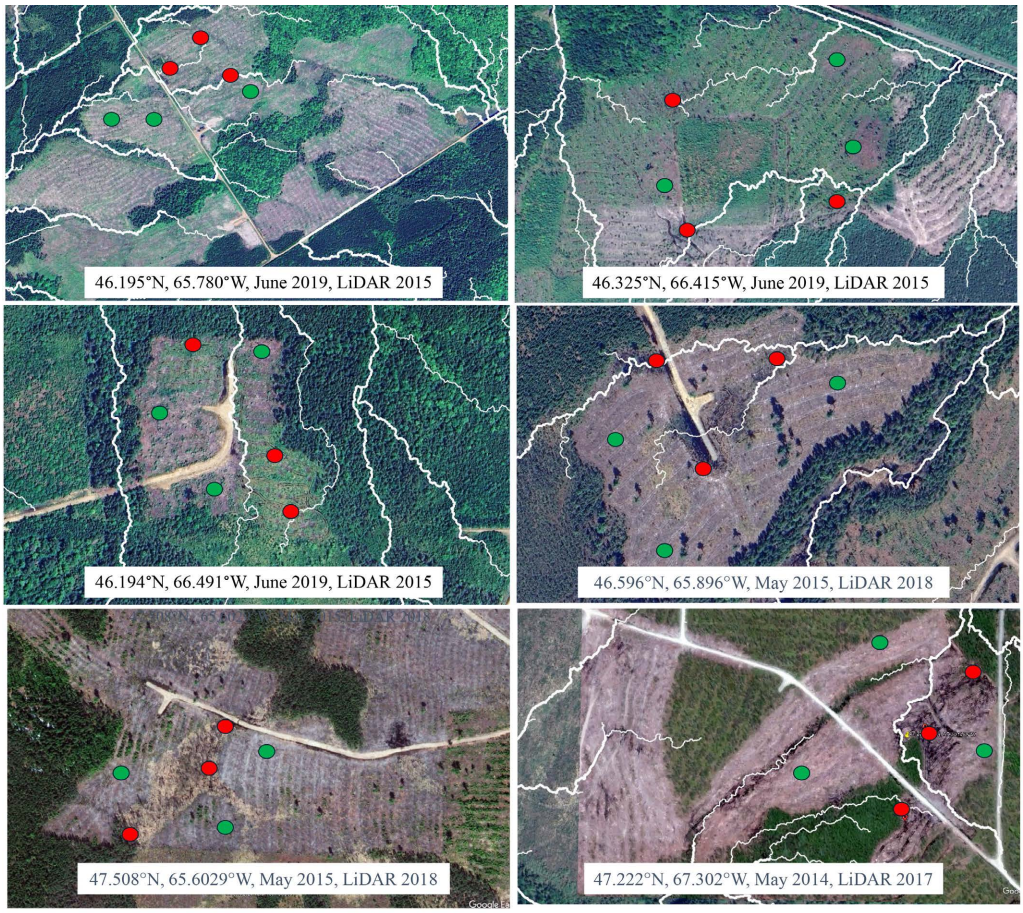

Figure 2. Cutblock rut (red) and no-rut (green) marking examples based on earliest post-harvest Google Earth imagery appearances by month and year, and the year of LiDAR DEM coverage as well. Also shown: harvest roads and white lines representing the DEM-derived flow channels with >1 ha (thin) and >4 ha (thick) upslope flow accumulation areas.

Table 1. Image-recognized in-block features that allow discerning ruts from non-rut features.

Feature Qualities	In-Block Features				
	Ruts	**Tree shadows**	**Non-rutted harvest trails**	**Naturally formed puddles**	**Slash piles**
Color	Dark	Dark	Light	Dark	Dark and light
Orientation	Any direction, but along harvest trails	Unidirectional	Any direction	Any direction	Any direction, or piled across harvest trails
Length/Width	Short to long, featuring tire footprints	Short/thin to wide	Long	Short/Wide	Short/short

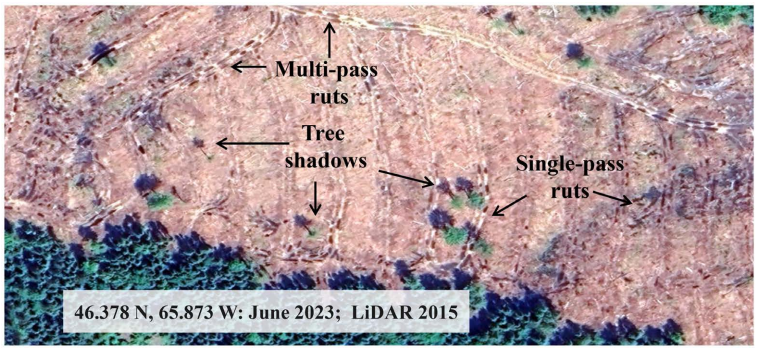

Figure 3. Discerning single-pass ruts from tree shadows and multi-pass ruts.

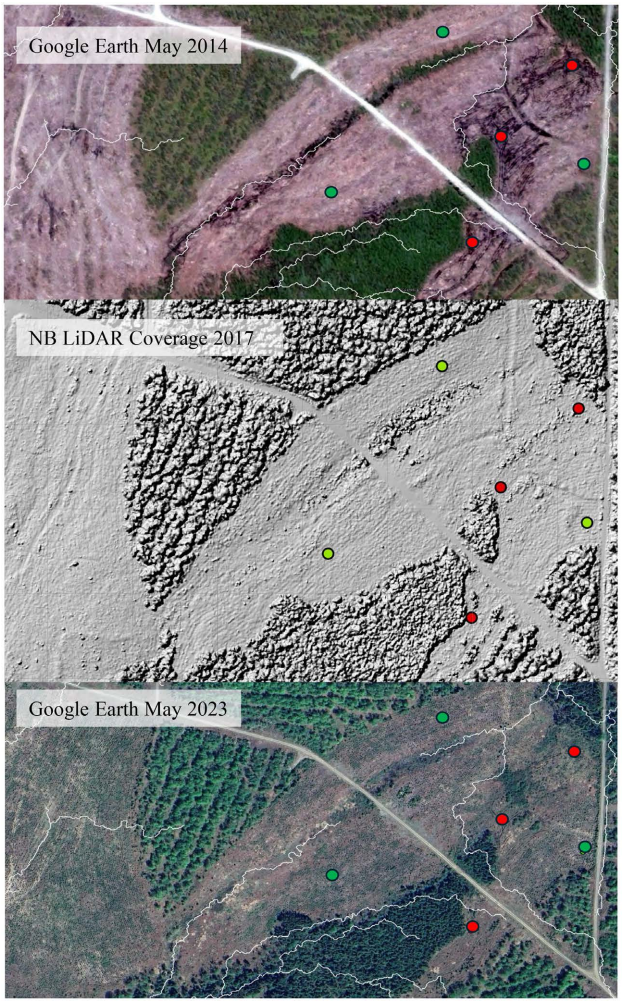

Figure 4. Example of single-pass rut marking within the context of water-filled rut conditions: 1) shortly after cutblock harvesting (top), 2) 9 years thereafter (bottom), and 3) in comparison with the hill-shaded LiDAR-derived full-feature elevations 3 years after harvesting (middle) with only the multi-pass trails and access roads remaining fully DEM apparent. Single-pass trails are not fully DEM resolved at 1 m resolution, and are—in places—overgrown by vegetation at imaging time. Overall vegetation recovery is slow but is more pronounced in the lower-lying areas. The underlying "Holmesville" soil represents a glacially compacted medium textured soil with shallow rooting depth and low coarse fragment content. Location: 47.222˚N, 67.301˚W.

2.3. Attribute Specifications for the Selected Rut and No-Rut Locations

The rut and no-rut location data within the AOE, AOV, and AOM study areas were subsequently supplemented with their DEM-generated depression, slope, flow direction, flow accumulation, flow channel, DTW, and TPI attributes, all generated via ArcGIS-based DEM processing, as follows:

- Depression depth (Sink depth, in m) = DEM − filled DEM using ArcMap's Fill and Raster Calculator functions.
- Flow direction (FD), based on D8 Flow Direction processing [28].
- Flow accumulation (FA, in ha), using the D8 Flow Accumulation function.
- Flow channels, determined by re-classifying cells with FA ≤ 4 ha and/or ≤1 ha as no data, and FA > 4 ha and >1 ha as 1, followed by using the Raster to Polyline function.
- Slope (in %), using the Slope function.
- TWI = log FA/tan (Slope) [24].
- TPI = DEM – mean focal 49 - 50 m annulus elevation around each DEM cell, in m [26].
- DTW, using the Cost distance function with Slope as cost raster and the >1 ha ("ephemeral") and >4 ha ("permanent") flow channels as DTW = 0 reference cells, in m [27].

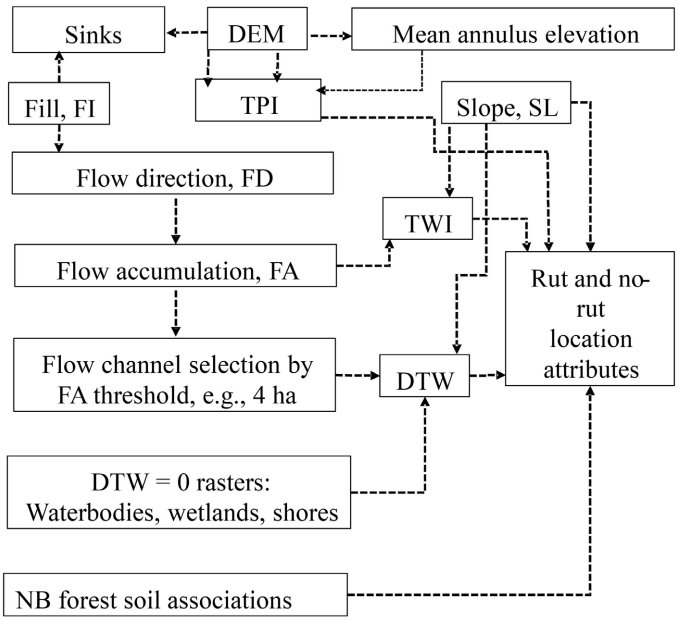

Figure 5. Workflow used to generate the attribute shapefiles for the selected rut-and no-rut locations for each of the three study areas in **Figure 1**.

These layers were used to determine Sink Depth, Slope, TWI, TPI, DTW, and Soil type for each rut and no-rut location. The results so obtained were then added to the rut and no-rut point shapefile using the Extract Multipoint tool. The Forest

Soil Map for New Brunswick had its 48 soil association mapping units identified at each rut/no-rut mapping point by 1 where present and 0 where not present. This was done after adjusting the areal extent of these units to correspond to GeoNB's current waterbody and wetland delineations. **Figure 5** summarizes the workflow used to determine the required rut and no-rut attributes for each location.

2.4. Rut versus No-Rut Probability Assessment

Logistic regression analysis was used to determine the extent to which the topographic and soil-based attributes determine rut occurrence probabilities within the marked cutblocks. This probability, symbolized by $P_{rut}(y)$, is estimated by setting:

$$P_{rut}(y) = 1/[1 + \exp(-y)]$$

where y represents the dependent binary number for each rut (1) and no-rut (0) location, and this number likely varies by the location-specific attributed as follows:

$$y = a + b\ TPI + c\ DTW_{FA>4ha} + d\ DTW_{FA>1ha} + e\ Slope + f\ TWI + g\ Sink + f\ (Soil\ Associations)$$

where a, b, c, d, e, f, g are the logistic regression coefficients, TPI, DTW, TWI, Sink, and f (Soil Associations) are the location-specific rut and non-rut attributes. In detail,

$$f\ (Soil\ Association) = S_{Ca}Ca + S_{Cr}Cr + S_{Re}Re + S_{Si}Se + \ldots,$$

in which S_{Ca}, S_{Cr}… refer to the soil-specific regression coefficients, and Ca, Cr, … refer to which soil association is present (1) or not (0) at each specific rut or non-rut location, and Ca, Cr, Re, and Se refer, e.g., to the Caribou, Carleton, Reece, and Siegas soil associations. To proceed, the resulting AOI, AOM, and AOV point shapefiles were converted into text files, and these were subsequently subjected to logistic regression analysis in Statview (https://speciation.net/Database/Components/SAS-Institute-Inc/StatView-;i1897).

3. Results and Discussion

The best-fitted logistic regression analysis results for the individual and combined study areas are summarized in **Table 2A**. As shown, the AOE and AOV results so obtained are nearly identical individually and combined, with TPI and $DTW_{FA>4ha}$ as the only significant rut occurrence predictor variables. In this, the similarity of the AOV to AOE results indicates that the AOE-generated rut occurrence predictions are, in principle, equally applicable to the much wider AOV area, and are therefore likely applicable across New Brunswick. The AOM results, however, differ from the AOE and AOV results by way of the AOM-enhanced and mostly TPI-based rut occurrence results. This suggests that using the AOM-derived model is based on guiding the image-based rut marking process deeper into the low-lying TPI locations. To that effect, a considerable number of ruts occurred within the

DTW< 1 m zonations along and next to the DEM-derived flow channels with >4 and >1 ha upslope flow accumulations.

Using TPI (Table 2B) as the only rut occurrence predictor variable slightly increased the number of false positives and negatives while lowering the overall correctness classification by 1.2%. In contrast, using only the $DTW_{FA>4ha}$ raster drastically reduced the correctness classification to 63.4% (Table 2C), therefore implicating TPI as the most significant rut occurrence predictor variable. In comparison, the Sink depth, Slope, TWI, and soil type data for the rut and no-rut locations were all found to be insignificant when used in combination with TPI and $DTW_{FA>4ha}$ as rut probability predictor variables.

Based on the Table 2A entries, the resulting rut occurrence probability function takes on the following form

$$P_{rut}(y) = 1/\{1 + \exp[-(-0.022 - 6.14\ TPI - 1.08 \log_{10}(DTW))]\}$$

with TPI and DTW = $DTW_{FA>4ha}$ or $DTW_{FA>1ha}$ all in m. This equation was subsequently applied across New Brunswick based on the provincial DEM-generated $DTW_{FA>4ha}$ and TPI data layers. The result of so doing is illustrated in Figure 6 by way of the traffic-light $P_{rut}(y)$ overlay on the six images in Figure 2 underneath the marked rut (red) and no-rut (green) locations.

Table 2. Best-fitted logistic regression results and related classification correctness that topographically relate the AOE-, AOV- and AOM-marked rut and no-rut occurrences to the TPI and DTW indices (A), to TPI alone (B), and to $DTW_{FA>4ha}$ alone (C), with $DTW_{FA>4ha}$ set equal to zero along stream channels with >4 ha upslope flow accumulation areas.

A

Study area		Regression Analysis					Logistic Classification: n and %				Overall Correct-ness
				Regression Coefficients			Observed 0		Observed 1		
		n	R^2	Constant	TPI	$\log_{10}$ (DTW)	Predicted 0	Predicted 1	Predicted 0	Predicted 1	
AOE	Estimate	2930	0.476	−0.18	−5.26	−1.19	1602	120	204	1004	89.5
	Std. Error			±0.06	±0.022	0.11					
	Chi-Square			10.6	652.1	112.2	54.7%	4.1%	7.0%	34.3%	
	P-Value			0.0011	<0.0001	<0.0001					
AOV	Estimate	980	0.690	0.43	−5.89	−1.29	471	19	28	462	94.3
	Std. Error			0.14	0.41	0.25					
	Chi-Square			9.72	204.0	25.9	48.1%	1.9%	2.9%	47.1%	
	P-Value			0.69	<0.0001	<0.0001					
AOM	Estimate	855	0.915	0.96	−13.9	−1.14	414	4	2	435	99.2
	Std. Error			0.28	1.5	0.67					
	Chi-Square			11.6	85.2	2.9	48.4%	0.5%	0.2%	50.9%	
	P-Value			0.0007	<0.0001	0.088					
Combined	Estimate	4765	0.580	0.022	−6.14	−1.08	2456	174	214	1921	92.0
	Std. Error			0.05	0.19	0.10					
	Chi-Square			0.189	1040.6	118.7	51.5%	3.7%	4.5%	40.3%	
	P-Value			0.684	<0.0001	<0.0001					

Continued

B										
Study area	**Regression Analysis**					**Logistic Classification: n and %**				**Overall Correct-ness**
		n	**R^2**	**Regression Coefficients**		**Observed 0**		**Observed 1**		
				Constant	TPI	Predicted 0	Predicted 1	Predicted 0	Predicted 1	
AOE	Estimate	2930	0.441	−0.24	−5.69	1590	132	212	996	88.3
	Std. Error			±0.05	±0.22					
	Chi-Square			20.5	682.9	54.3%	4.5%	7.2%	34.0%	
	P-Value			<0.0001	<0.0001					
AOV	Estimate	980	0.667	0.26	−6.4	463	27	30	460	94.2
	Std. Error			0.12	0.42					
	Chi-Square			4.49	229.3	47.2%	2.8%	3.1%	46.9%	
	P-Value			0.034	<0.0001					
AOM	Estimate	855	0.912	1.01	−14.12	413	5	3	434	99.1
	Std. Error			0.28	1.48					
	Chi-Square			13.3	91.5	48.3%	0.6%	0.4%	50.8%	
	P-Value			0.0003	<0.0001					
Combined	Estimate	4765	0.558	−0.07	−6.50	2447	183	219	1916	91.2
	Std. Error			0.05	0.19					
	Chi-Square			2.47	1153.3	51.4%	3.8%	4.6%	40.2%	
	P-Value			0.116	<0.0001					

C										
Study area	**Regression Analysis**					**Logistic Classification: n and %**				**Overall Correct-ness**
		n	**R^2**	**Regression Coefficients**		**Observed 0**		**Observed 1**		
				Constant	$\log_{10}$ (DTW)	Predicted 0	Predicted 1	Predicted 0	Predicted 1	
AOE	Estimate	2930	0.129	−0.209	−1.62	1509	213	670	538	69.9
	Std. Error			0.042	0.09					
	Chi-Square			24.5	348.6	51.5%	7.3%	22.9%	18.4%	
	P-Value			<0.0001	<0.0001					
AOV	Estimate	980	0.153	0.314	−1.65	354	136	181	309	67.7
	Std. Error			0.079	0.14					
	Chi-Square			15.8	133.9	36.1%	13.9%	18.5%	31.5%	
	P-Value			<0.0001	<0.0001					
AOM	Estimate	855	0.11	0.72	−2.01	289	129	184	253	63.4
	Std. Error			0.11	0.21					
	Chi-Square			42.5	87.8	33.8%	15.1%	21.5%	29.6%	
	P-Value			<0.0001	<0.0001					
Combined	Estimate	4765	0.119	0.029	−1.56	2172	458	1090	1045	67.5
	Std. Error			0.034	0.06					
	Chi-Square			0.737	539.9	45.6%	9.6%	22.9%	21.9%	
	P-Value			0.391	<0.0001					

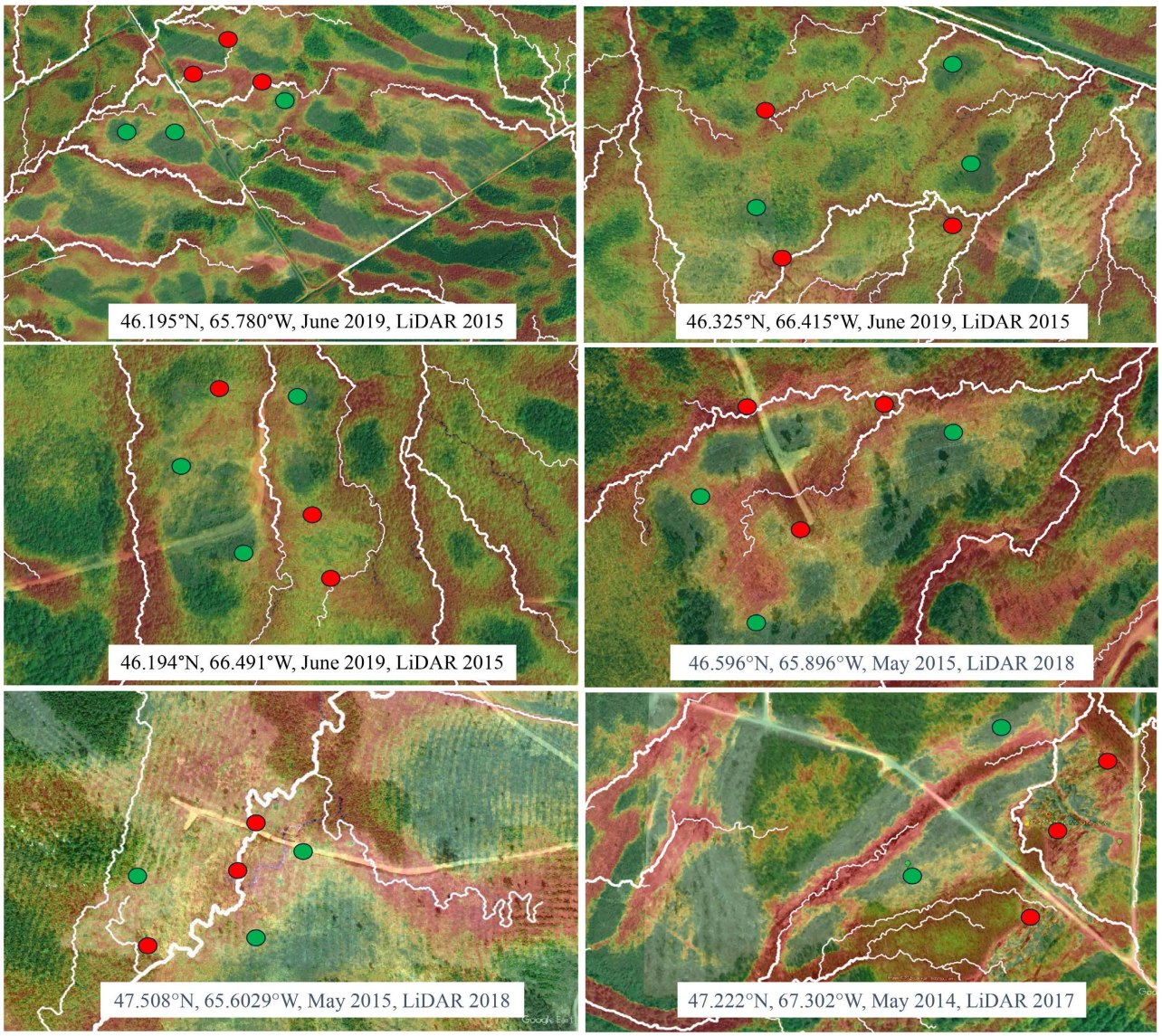

Figure 6. Overlay of the 0 (green) to 1 (red) rut occurrence probability pattern underneath the marked rut (red) and no-rut (green) locations on the image panels in **Figure 2**, with yellow-colored $P_{rut}(y) \approx 0.5$ transition zones.

The following can be observed from **Figure 6**:

- The $P_{rut}(y)$-projected red-to-green projections generally portray, respectively, the uphill recharge and the downhill discharge zones.
- The DEM-derived flow channels with FA > 1 ha generally occur within the red zones.
- Image-discernable ruts mainly occur within the red zones, and more so in the deeper lying area, where soil-saturating water would prevail for longer periods of time.
- Single-pass ruts may also occur outside the reddish zones, including flat areas where TPI and $P_{rut}(y)$ trend towards to or remain at ≈0 and ≈0.5, respectively.
- In contrast to single-pass ruts, multi-pass ruts can often be traced across the red-to-yellow-to-green zonations. Typically, these ruts are more pronounced

in the red zone while fading towards the yellow and green zones due to DTW-expected changes in moisture-affecting soil compaction.

Figure 7 illustrates how the $P_{rut}(y)$ projected red-to-yellow and green zones (Panels E, F) relate to 1) Google Earth images for August 2021 and May 2023 for a select location (Panels A and B), 2) the corresponding change in elevation (Panel C), and 3) the resulting $DTW_{A>4ha}$ pattern (Panel D). Note that the area at the and of the logging road in Panel A transits from dark to yellow and green in June 2021, but not so in May 2023. These changes reflect the re-foliation extent in June, and the lack thereof in May. The dark area is due to the presence of water-filled ruts due to the road-blocked west-to-east flow pattern.

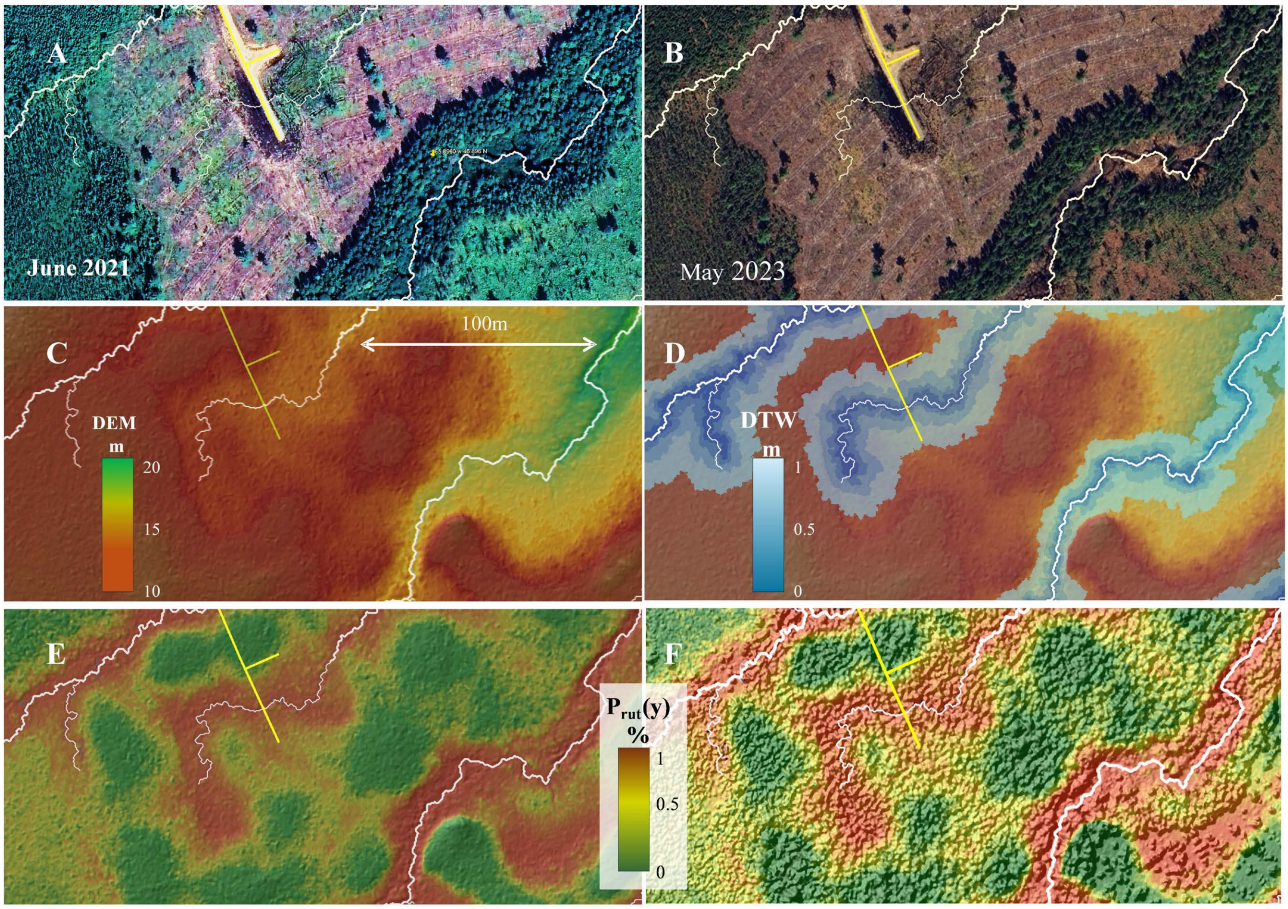

Figure 7. An example of post-harvest August 2021 and May 2023 Google Earth cutblock images (A, B), the corresponding LiDAR-derived DEM and $DTW_{FA>1ha}$ < 1 m patterns (C, D), and the $P_{rut}(y)$-generated rut probability projection when overlaid on the hill-shaded DEM (E) and the LiDAR-generated hillshaded pre-harvest canopy height pattern (F). Also shown: DEM-derived flow channels (white) with >4 ha (thick lines) and >1 ha (thin lines) upslope flow-accumulation areas. Location: 65.896W, 46.896N.

The overlay of the $P_{rut}(y)$ projection on the hillshaded canopy height Panel F may provide insights in terms of (e.g.):

- improving pre-harvest access road and wood landing placements, with further intent to minimize inadvertent trail-induced flow blockages and rutting;
- developing harvest trail layouts and deciding on operations timing, to optimize

on- and off-road trafficability when the ground within cutblocks is moist to wet and unfrozen;

- optimizing the timing and zoning of post-harvest operations.

Figure 8 presents another example of the $P_{rut}(y)$-generated red to green zonation with the DEM-derived FA > 1 ha flow channels and associated $DTW_{FA>1ha}$ < 1 m overlaid. Also included are the DEM and DEM-$DTW_{FA>1ha}$ profile lines which connect 10 individually dug soil pits. The observed soil drainage conditions, judged by depth of mottle appearances, varied from poor at Location 8, to imperfect at Locations 6, 9, and 10, moderate at Locations 1 and 2, and well at Locations 3, 4, 5 and 7.

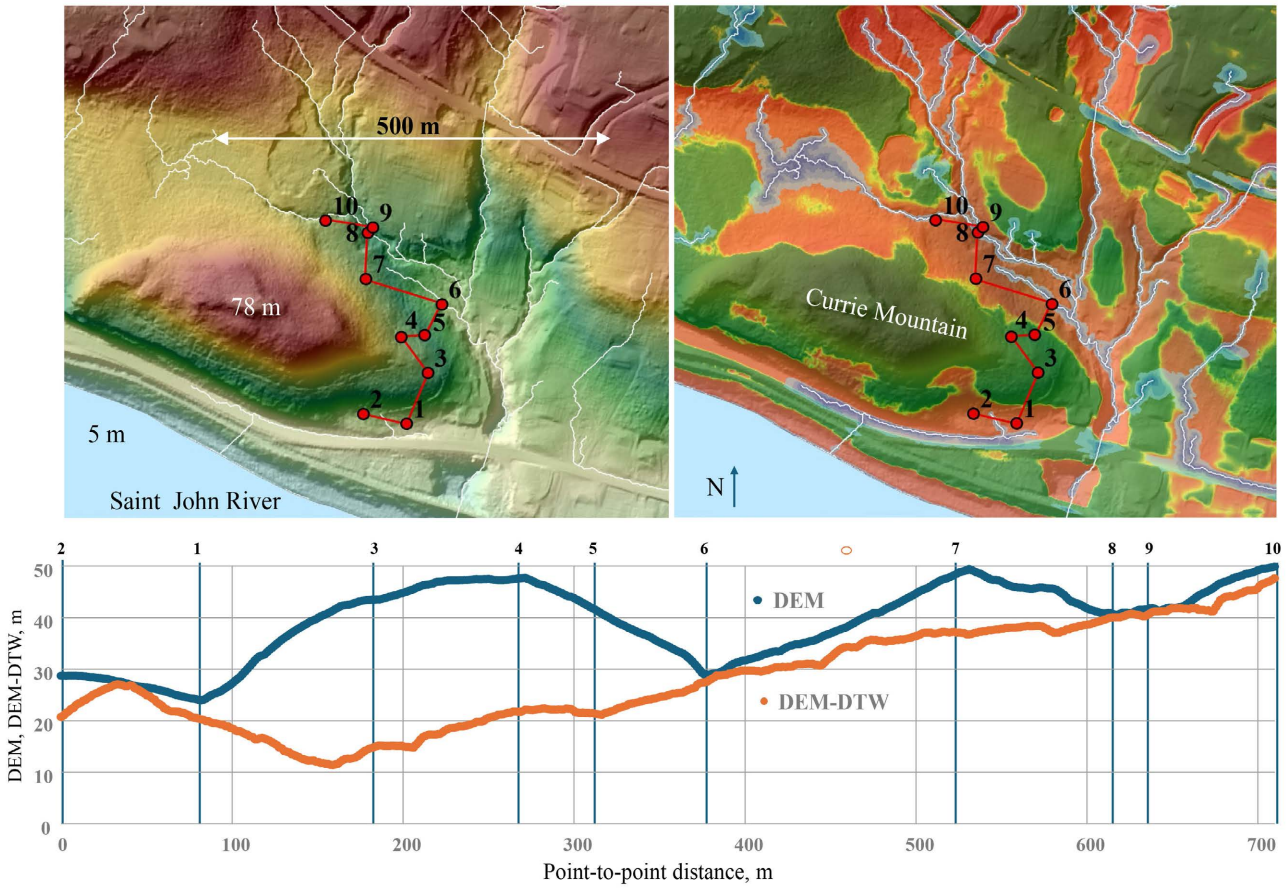

Figure 8. Hillshaded DEM (top left) and corresponding $P_{rut}(y)$ projection regarding potential rut (red) and no-rut (green) occurrences (top right), overlaid by the DEM-derived FA > 1 ha flow channels, and the associated blue-shaded $DTW_{FA>1ha}$ < 1 m layer. Also shown: 1) red dots numbered 1 to 10 referring to individually dug soil pits, done to assess the depths of mottle appearances as location-specific soil drainage indicators; 2) the corresponding point-to-point DEM and DEM-DTW elevation profiles (bottom). Location: 66.753W, 45.983N.

Figure 9 confirms that ruts—where they occur—are generally found within the lower-lying stream-supporting parts of the $P_{rut}(y)$-projected high rut-occurrence zones. In addition, these zones connect smoothly across the land from one stream to the next. The two examples in Figure 9 show that this remains so as the terrain changes from gently sloping (left side) to being highly irregular (right side) while

the elevational variations for these examples remain within 20 m across their areal extent.

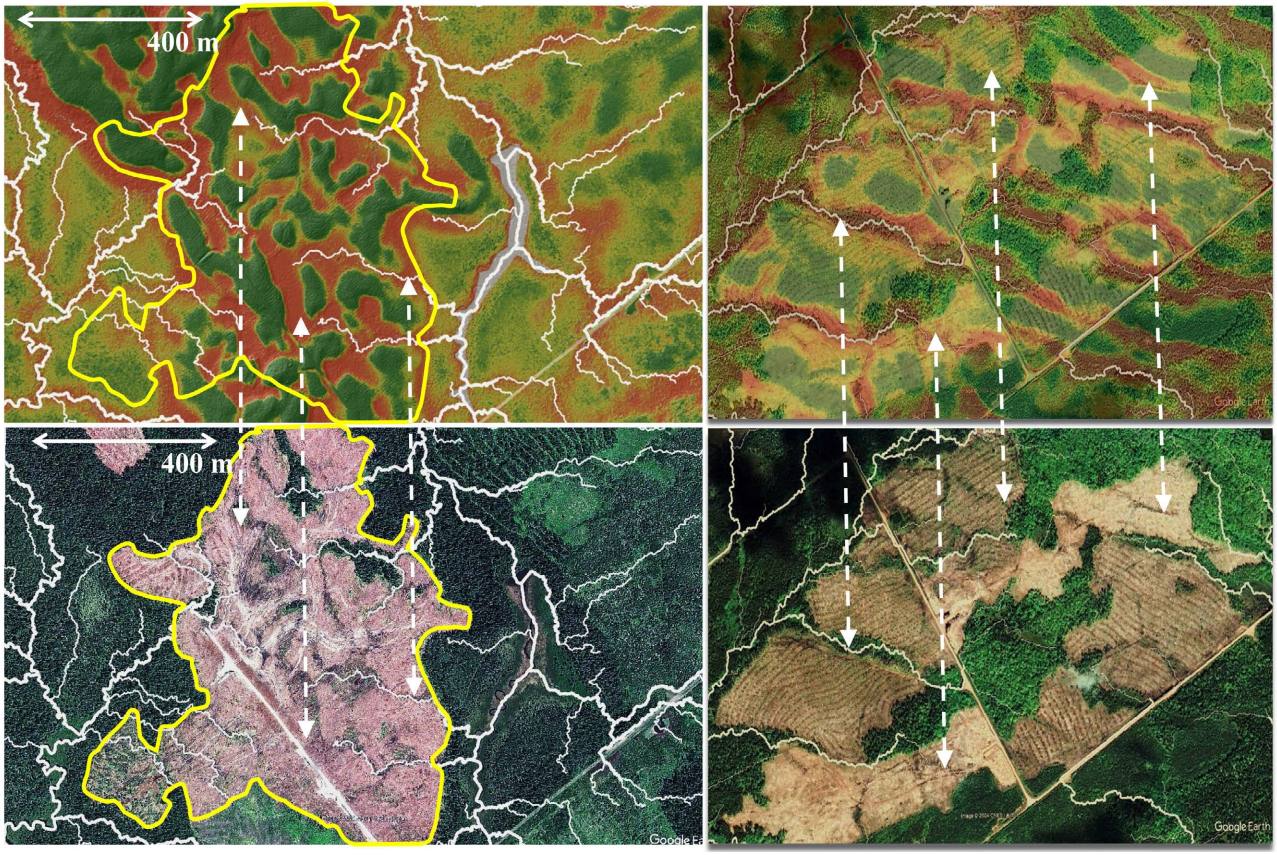

Figure 9. $P_{rut}(y)$ projected rut occurrence zones (top) across a gently sloped (left) and a highly irregular (right) terrain in comparison with the corresponding Google Earth images (bottom). Example on the left: 46.195N, 65.780W; Google Earth Image June 2019. Example on the right: 47.322N, 67.755W; Google Earth Image June 2010. White lines: DEM-delineated stream channels with >1 ha FA (thin) and >4 ha FA (thick). Stippled lines: one-on-one correspondence guides.

Figure 10 provides an example where the $P_{rut}(y)$ projection fails to project actual rut occurrences. This is seen to occur along an up to 5-m incised train track along its adjacent flat terrain. This caused the derivation of the TPI index to remain positive across this terrain therefore rendering the $P_{rut}(y)$ projections to be near 0%, and therefore no-rut predictive up to about 30 m on either side of the track. Similar situations would occur along other deeply incised landscape-affecting features such as flat terrains incised by highways, steep shores, and/or river channels.

Elsewhere on nearly flat ground such as table tops and wetlands, TPI projections vary around zero by definition, thereby rendering the resulting $P_{rut}(y)$ projections transitional and to be rut and no-rut predictive at 50% - 50%. Where this occurs, overlaying the DEM-derived 10-m smoothed slope layer on ortho images reveals that image-recognized ruts become increasingly more visible as the slopes decrease from 6% to 0% (**Figure 11**).

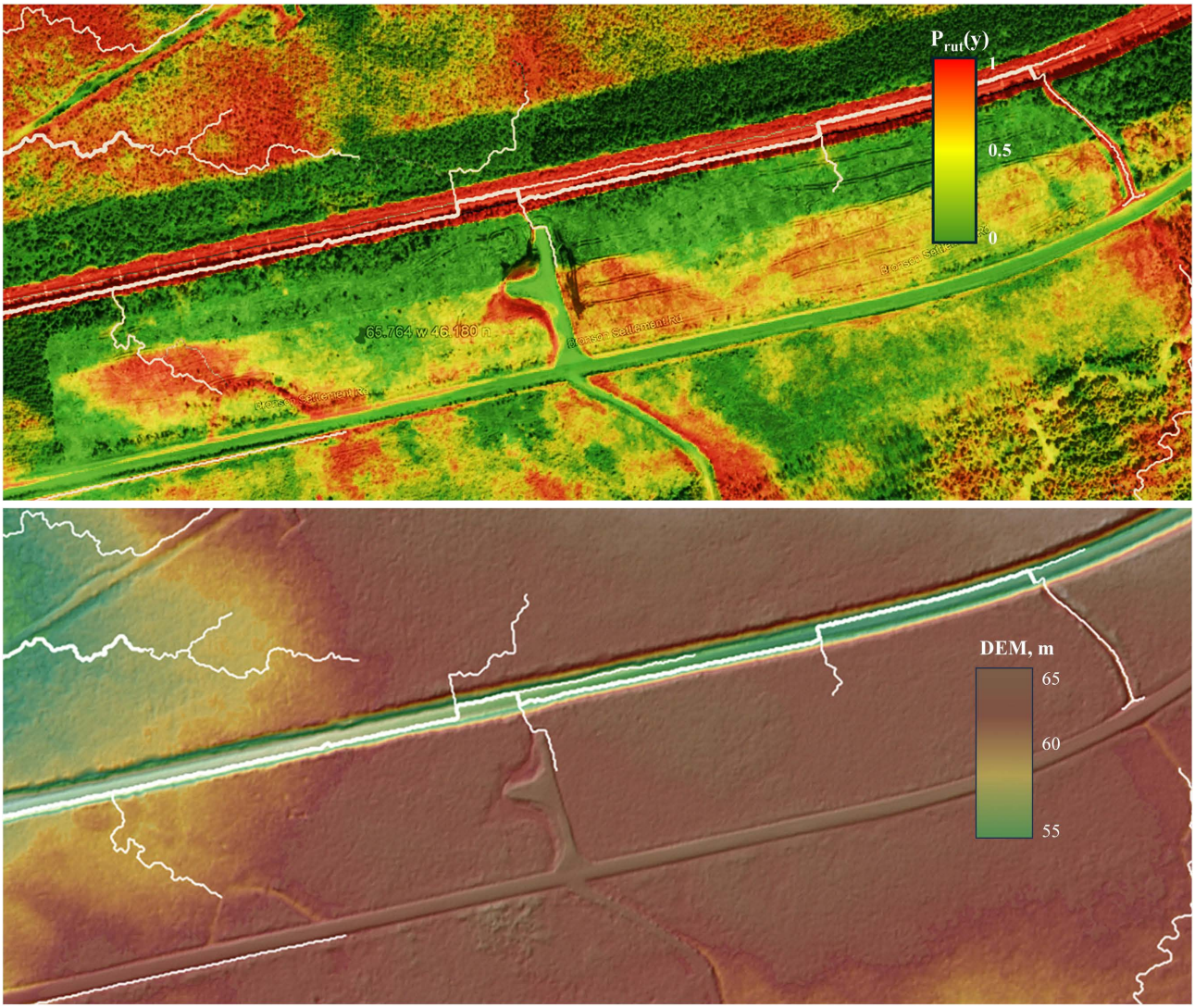

Figure 10. Top: Example of a false $P_{rut}(y)$ no-rut projection situation as found on a flat terrain within 30 m due to the impact of the 5-m incised train track on the TPI calculations. In contrast, also note the general low to absent influence of the slightly elevated road running parallel south of the train track. Location: 46.180, −65.764; Google Earth Image: June 2019; Bottom: LiDAR-DEM 2015.

Note that the $P_{rut}(y)$ projections do not only apply to the rut versus no-rut marking extent as portrayed in **Figure 1**, but also apply to locating rut-prone cutblock operations across New Brunswick and elsewhere. This is demonstrated in **Figure 12**, showing two Google-Earth located cutblock examples in Nova Scotia, with corresponding $P_{rut}(y)$ rut probability projections, but with the TPI and $DTW_{FA>1ha}$ combination as the y-predictor variables. The reason for selecting $DTW_{FA>1ha}$ instead of $DTW_{FA>4ha}$ relates to the fact that mean annual precipitation levels generally increase from 1000 mm/ha across New Brunswick to 1500 mm/ha across southwestern Nova Scotia, thereby enhancing the intensity of operation-induced soil rutting along ephemeral flow channels.

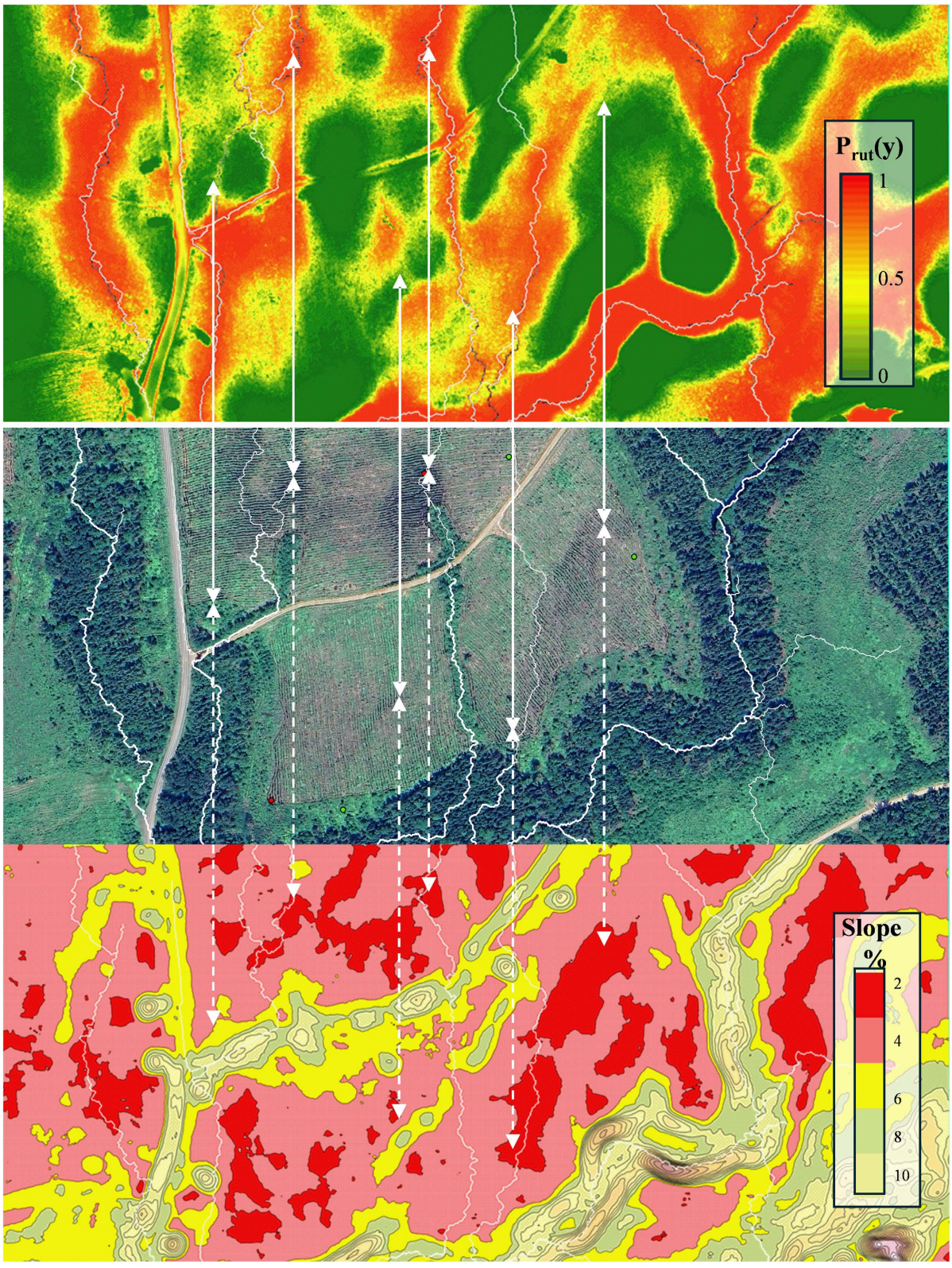

Figure 11. An example where the diminishing slope of the DEM-derived 10-m slope layer (bottom) can be used to center on image-discernable rut occurrences (middle) where $P_{rut}(y)$ also projects probable rut and no-rut occurrences at 50% (top) due to nearly flat ground conditions. Stippled lines: one-on-one location correspondence guides. Location: 45.907N, 65. 641W; Google Earth Image: July 2023.

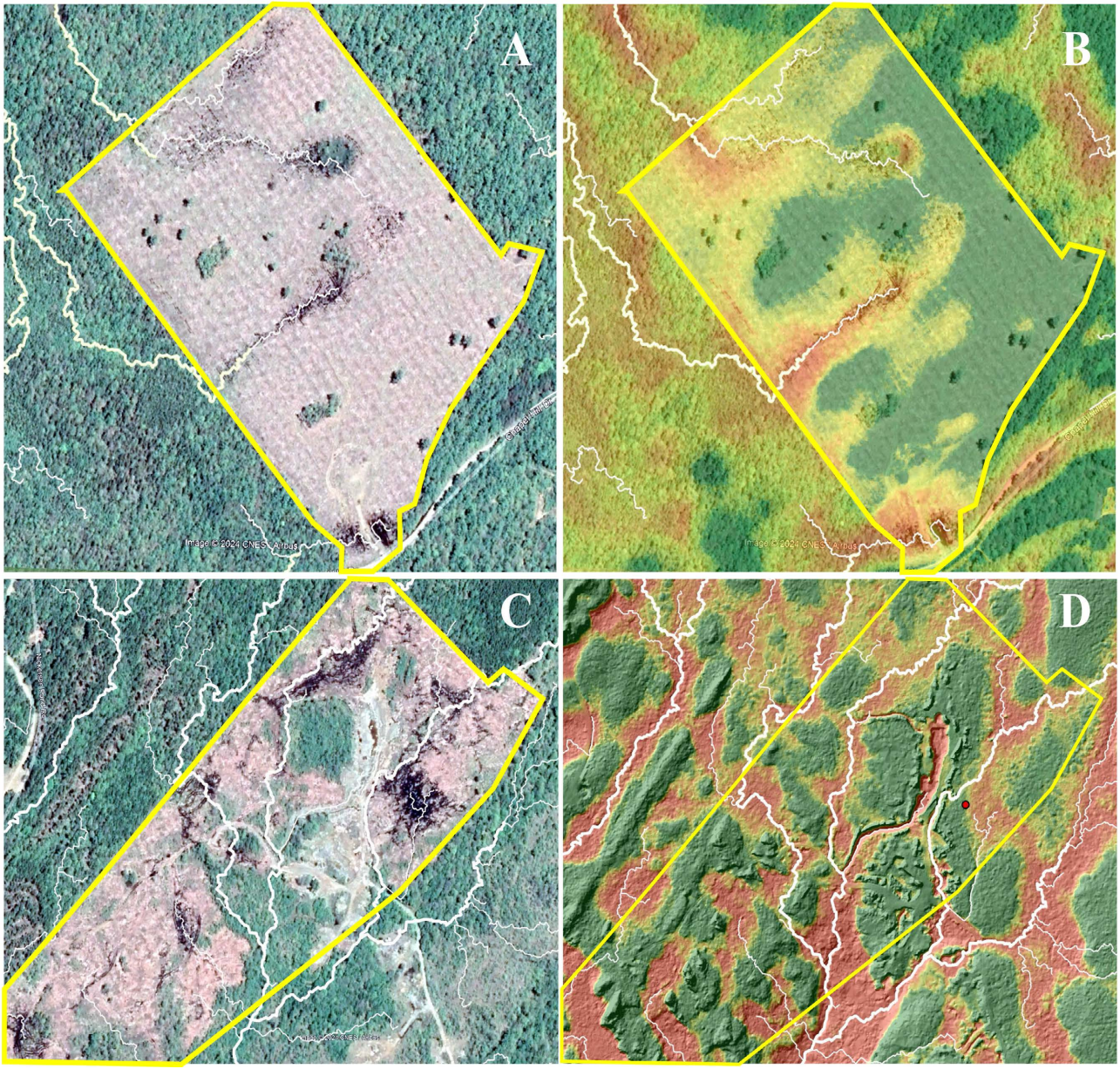

Figure 12. Google Earth images (June 2019, Panels A, C) for two cutblock locations in southwestern Nova Scotia (44.271N, 64.865W, top; 44.078N, 64.689W, bottom), also with the corresponding $P_{rut}(y)$ generated rut-zonation projections overlayed on the image (Panel B) on the hillshaded DEM (Panels D). White lines: flow channels with FA > 1 (thin) and >4 ha (thick). Cutblock outlines: yellow).

In addition to rut occurrences in cutblocks, $P_{rut}(y)$ projections reveal where roads, trails, powerlines, and pipelines also incur rutting. This is demonstrated in **Figure 13**, showing corridor-centered rut occurrences within the $P_{rut}(y)$-projected rutting zones. As can be verified, the same pattern recurs when and where the corridor-locating images are bare, wet, and unfrozen. This being so, the above methodology can be used to map and address matters pertaining to, e.g., corridor access and related on- and off-road trafficability and maintenance requirements.

Figure 13. Google Earth image (April 2024; top) featuring an intersection of a highway, a pipeline, a powerline and trails overlayed with the corresponding $P_{rut}(y)$ green-yellow-red rut-zonation projections (bottom). Location: 46.184N, 64.607W, in southeastern New Brunswick.

4. Concluding Remarks

It appears that the $P_{rut}(y)$ projections, apart from delineating single-pass rut versus no-rut occurrence zones, can also be interpreted as a DEM-generated way to delineate discharge versus recharge zonation. As such, the $P_{rut}(y)$-projected rut-occurrence zones represent downslope water-accumulating areas where machine-incurred ruts become prevalent while operating on wet and unfrozen soils.

The above rut-marking approach provides no information on the depth of the ruts. Rut depths would generally be shallowest in upslope positions and deepest in downhill water-saturated areas. As reported elsewhere (e.g., [5] [6] [31]-[34]), rut depths depend on machine load, number of passes, tire or track footprint pressure, the timing of the operations, and the resistance of the soil to compaction as affected by upslope to downslope changes in soil density, texture, presence of coarse fragments, and soil moisture content. Additional rut deepening would be

incurred along uphill tracks due to increased tire traction [35]. Further research is required to determine which soil types prove to be more conducive to rutting specifically. Doing so would require marking and evaluating rut and no-rut locations when incurred across varying soil types during same or similar weather and machine-operating conditions.

Conflicts of Interest

The authors declare no conflicts of interest regarding the publication of this paper.

References

[1] Naghdi, R., Bagheri, I., Lotfalian, M. and Setodeh, B. (2009) Rutting and Soil Displacement Caused by 450C Timber Jack Wheeled Skidder (Asalem Forest Northern Iran). *Journal of Forest Science*, **55**, 177-183. https://doi.org/10.17221/102/2008-jfs

[2] Cambi, M., Certini, G., Neri, F. and Marchi, E. (2015) The Impact of Heavy Traffic on Forest Soils: A Review. *Forest Ecology and Management*, **338**, 124-138. https://doi.org/10.1016/j.foreco.2014.11.022

[3] Solgi, A., Naghdi, R. and Nikooy, M. (2016) Effects of Skidderon Soil Compaction, Forest Floor Removal and Rut Formation. *Madera y Bosques*, **21**, 147-155. https://doi.org/10.21829/myb.2015.212451

[4] Uusitalo, J., Ala-Ilomäki, J., Lindeman, H., Toivio, J. and Siren, M. (2020) Predicting Rut Depth Induced by an 8-Wheeled Forwarder in Fine-Grained Boreal Forest Soils. *Annals of Forest Science*, **77**, Article No. 42. https://doi.org/10.1007/s13595-020-00948-y

[5] Labelle, E.R., Hansson, L., Högbom, L., Jourgholami, M. and Laschi, A. (2022) Strategies to Mitigate the Effects of Soil Physical Disturbances Caused by Forest Machinery: A Comprehensive Review. *Current Forestry Reports*, **8**, 20-37. https://doi.org/10.1007/s40725-021-00155-6

[6] Jones, M. and Arp, P. (2019) Soil Trafficability Forecasting. *Open Journal of Forestry*, **9**, 296-322. https://doi.org/10.4236/ojf.2019.94017

[7] Marra, E., Cambi, M., Fernandez-Lacruz, R., Giannetti, F., Marchi, E. and Nordfjell, T. (2018) Photogrammetric Estimation of Wheel Rut Dimensions and Soil Compaction after Increasing Numbers of Forwarder Passes. *Scandinavian Journal of Forest Research*, **33**, 613-620. https://doi.org/10.1080/02827581.2018.1427789

[8] Marra, E., Laschi, A., Fabiano, F., Foderi, C., Neri, F., Mastrolonardo, G., *et al.* (2021) Impacts of Wood Extraction on Soil: Assessing Rutting and Soil Compaction Caused by Skidding and Forwarding by Means of Traditional and Innovative Methods. *European Journal of Forest Research*, **141**, 71-86. https://doi.org/10.1007/s10342-021-01420-w

[9] Mohieddinne, H., Brasseur, B., Gallet-Moron, E., Lenoir, J., Spicher, F., Kobaissi, A., *et al.* (2022) Assessment of Soil Compaction and Rutting in Managed Forests through an Airborne LiDAR Technique. *Land Degradation & Development*, **34**, 1558-1569. https://doi.org/10.1002/ldr.4553

[10] Pirnazarov, A., Wijekoon, M., Sellgren, U., Löfgren, B. and Andersson, K. (2012) Modeling of the Bearing Capacity of Nordic Forest Soil. *Proceedings of the* 12*th European Regional Conference of the International Society for Terrain-Vehicle Systems*, Pretoria, 24-27 September 2012, 1-12.

[11] Ampoorter, E., Van Nevel, L., De Vos, B., Hermy, M. and Verheyen, K. (2010) As-

sessing the Effects of Initial Soil Characteristics, Machine Mass and Traffic Intensity on Forest Soil Compaction. *Forest Ecology and Management*, **260**, 1664-1676. https://doi.org/10.1016/j.foreco.2010.08.002

[12] Nugent, C., Kanali, C., Owende, P.M.O., Nieuwenhuis, M. and Ward, S. (2003) Characteristic Site Disturbance Due to Harvesting and Extraction Machinery Traffic on Sensitive Forest Sites with Peat Soils. *Forest Ecology and Management*, **180**, 85-98. https://doi.org/10.1016/s0378-1127(02)00628-x

[13] Sirén, M., Salmivaara, A., Ala-Ilomäki, J., Launiainen, S., Lindeman, H., Uusitalo, J., *et al.* (2019) Predicting Forwarder Rut Formation on Fine-Grained Mineral Soils. *Scandinavian Journal of Forest Research*, **34**, 145-154. https://doi.org/10.1080/02827581.2018.1562567

[14] Sutherland, B.J. (2003) Preventing Soil Compaction and Rutting in the Boreal Forest of Western Canada: A Practical Guide to Operating Timber-Harvesting Equipment. Forest Engineering Research Institute of Canada (FERIC).

[15] Horn, R., Vossbrink, J. and Becker, S. (2004) Modern Forestry Vehicles and Their Impacts on Soil Physical Properties. *Soil and Tillage Research*, **79**, 207-219. https://doi.org/10.1016/j.still.2004.07.009

[16] Horn, R., Vossbrink, J., Peth, S. and Becker, S. (2007) Impact of Modern Forest Vehicles on Soil Physical Properties. *Forest Ecology and Management*, **248**, 56-63. https://doi.org/10.1016/j.foreco.2007.02.037

[17] Zemke, J. (2016) Runoff and Soil Erosion Assessment on Forest Roads Using a Small Scale Rainfall Simulator. *Hydrology*, **3**, Article 25. https://doi.org/10.3390/hydrology3030025

[18] Allman, M., Jankovský, M., Messingerová, V., Allmanová, Z. and Ferenčík, M. (2015) Soil Compaction of Various Central European Forest Soils Caused by Traffic of Forestry Machines with Various Chassis. *Forest Systems*, **24**, e038. https://doi.org/10.5424/fs/2015243-07541

[19] Grigal, D.F. (2000) Effects of Extensive Forest Management on Soil Productivity. *Forest Ecology and Management*, **138**, 167-185. https://doi.org/10.1016/s0378-1127(00)00395-9

[20] Meek, P. (1996) Effects of Skidder Traffic on Two Types of Forest Soils. Technical Report No. TR-117, Forest Engineering Research Institute of Canada, Pointe-Claire.

[21] Saarilahti, M. and Anttila, T. (1999) Rut Depth Model for Timber Transport on Moraine Soils. *Proceedings of the 9th International Conference of International Society for Ter-rain Vehicle Systems*, Munich, 14-17 September 1999, 29-37.

[22] Vega-Nieva, D.J., Murphy, P.N.C., Castonguay, M., Ogilvie, J. and Arp, P.A. (2009) A Modular Terrain Model for Daily Variations in Machine-Specific Forest Soil Trafficability. *Canadian Journal of Soil Science*, **89**, 93-109. https://doi.org/10.4141/cjss06033

[23] Houle, D., Duchesne, L., Ouimet, R., Paquin, R., Meng, F. and Arp, P.A. (2002) Evaluation of the FORHYM2 Model for Prediction of Hydrologic Fluxes and Soil Temperature at the Lake Clair Watershed (Duchesnay, Quebec). *Forest Ecology and Management*, **159**, 249-260. https://doi.org/10.1016/s0378-1127(01)00438-8

[24] Sørensen, R., Zinko, U. and Seibert, J. (2006) On the Calculation of the Topographic Wetness Index: Evaluation of Different Methods Based on Field Observations. *Hydrology and Earth System Sciences*, **10**, 101-112. https://doi.org/10.5194/hess-10-101-2006

[25] Bretreger, D., Yeo, I. and Melchers, R. (2021) Terrain Wetness Indices Derived from Lidar to Inform Soil Moisture and Corrosion Potential for Underground Infrastruc-

ture. *Science of the Total Environment*, **756**, Article 144138. https://doi.org/10.1016/j.scitotenv.2020.144138

[26] Weiss, A. (2001) Topographic Position and Landforms Analysis. *Poster Presentation*, *ESRI User Conference*, San Diego, 9-13 July 2001.

[27] Murphy, P.N.C., Ogilvie, J., Meng, F., White, B., Bhatti, J.S. and Arp, P.A. (2011) Modelling and Mapping Topographic Variations in Forest Soils at High Resolution: A Case Study. *Ecological Modelling*, **222**, 2314-2332. https://doi.org/10.1016/j.ecolmodel.2011.01.003

[28] Tarboton, D.G. (1997) A New Method for the Determination of Flow Directions and Upslope Areas in Grid Digital Elevation Models. *Water Resources Research*, **33**, 309-319. https://doi.org/10.1029/96wr03137

[29] De Reu, J., Bourgeois, J., Bats, M., Zwertvaegher, A., Gelorini, V., De Smedt, P., *et al.* (2013) Application of the Topographic Position Index to Heterogeneous Landscapes. *Geomorphology*, **186**, 39-49. https://doi.org/10.1016/j.geomorph.2012.12.015

[30] Colpitts, M.C., Fahmy, S.H., MacDougall, J.E., Ng, T.T.M., McInnis, B.G. and Zelazny, V.F. (1995) Forest Soils of New Brunswick. CLBRR Contribution No. 95-38.

[31] Bygdén, G., Eliasson, L. and Wästerlund, I. (2003) Rut Depth, Soil Compaction and Rolling Resistance When Using Bogie Tracks. *Journal of Terramechanics*, **40**, 179-190. https://doi.org/10.1016/j.jterra.2003.12.001

[32] Toivio, J., Helmisaari, H., Palviainen, M., Lindeman, H., Ala-Ilomäki, J., Sirén, M., *et al.* (2017) Impacts of Timber Forwarding on Physical Properties of Forest Soils in Southern Finland. *Forest Ecology and Management*, **405**, 22-30. https://doi.org/10.1016/j.foreco.2017.09.022

[33] Jones, M. and Arp, P.A. (2017) Relating Cone Penetration and Rutting Resistance to Variations in Forest Soil Properties and Daily Moisture Fluctuations. *Open Journal of Soil Science*, **7**, 149-171. https://doi.org/10.4236/ojss.2017.77012

[34] Poltorak, B.J., Labelle, E.R. and Jaeger, D. (2018) Soil Displacement during Ground-Based Mechanized Forest Operations Using Mixed-Wood Brush Mats. *Soil and Tillage Research*, **179**, 96-104. https://doi.org/10.1016/j.still.2018.02.005

[35] Jones, M., Castonguay, M., Jaeger, D. and Arp, P. (2018) Track-Monitoring and Analyzing Machine Clearances during Wood Forwarding. *Open Journal of Forestry*, **8**, 297-327. https://doi.org/10.4236/ojf.2018.83020